Journal of Alloys and Compounds 853 (2021) 157233

Contents lists available at ScienceDirect

Journal of Alloys and Compounds

journal homepage: http://www.elsevier.com/locate/jalcom

Anelastic and viscoplastic deformation in a Fe-based metallic glass

C.C. Yuan *, R. Liu , C.M. Pang , X.F. Zuo , B.F. Li , S.C. Song , J.Y. Hu , W.W. Zhu , B.L. Shen **

School of Materials Science and Engineering, Jiangsu Key Laboratory for Advanced Metallic Materials, Southeast University, Nanjing, 211189, China

ARTICLE INFO

Article history:
Received 2 July 2020
Received in revised form
29 August 2020
Accepted 15 September 2020
Available online 16 September 2020

Keywords:
Creep
Anelastic and viscoplastic deformation
Disordered structure
Metallic glass

ABSTRACT

The micro-creep behavior of the $Fe_{66}Tb_5B_{23}Nb_6$ metallic glass and its anelastic and viscoplastic deformation mechanism were investigated by using nanoindentation. The Maxwell-Voigt model with one or two Kelvin units were utilized to describe three stages of creep deformations at different loading rates and temperatures during the constant load holding process. The creep displacement of the indenter into the $Fe_{66}Tb_5B_{23}Nb_6$ sample at a constant load obeys the classic relaxation kinetics at loading rates ranging from 5 to 100 mN s^{-1}. The activation energy for the relaxation process increases with increasing loading rate, which leads to the pronounced relaxation with longer characteristic times under a low-velocity impact mode observed at room temperature. On the other hand, the relaxation process with a short characteristic time plays a dominant role in determining viscoplastic flow and softening behavior at the temperature approaching the glass transition temperature. This work reveals the important role of the anelasticity on the plastic flow of metallic glasses under dynamic loading conditions.

1. Introduction

Nanomoulding facilitates a low-cost fabrication of micro- and nano-devices by thermoplastic imprinting glassy materials such as metallic glasses (MGs), especially those with low glass transition temperature (T_g) [1]. It is well documented that bulk MGs will be sharply softened when they are heated to the temperature between T_g and crystallization temperature (T_x) (i.e., the so-called supercooled liquid region, or ΔT) [2], even though the well-known high strength and hardness (H) at ambient temperature [3]. This softening process can help in manufacturing parts with complex shapes at the sub-micrometer or nanometer scale that traditional crystalline metals or techniques can barely achieve [4–7], which makes MGs as a promising candidate for thermoplastic nanomoulding. Nevertheless, a few studies are performed on imprinting, embossing, and molding of MGs with high T_g such as Fe-based MGs that normally exhibit a narrow ΔT and poor glass-forming ability [8–10]. Acknowledged as an excellent soft magnetic material, Fe-based MGs have been widely used in the field of power and electronics industries, demonstrating a wide range of applications and potential commercial value [11]. Previous work shows that microalloying of rare-earth (RE) elements can effectively enhance the thermal stability of Fe (Co)-based MGs [12–15] by suppressing the precipitation of metastable $Fe_{23}B_6$ and α-Fe crystalline phases [16]. For instance, Fe–B–Nb-RE (RE = Dy, Ho, Er, or Tm) bulk MGs with tunable Curie temperatures exhibit a wide ΔT close to 100 K and critical diameters up to 4.5 mm [17]. $(Co_{0.5}Fe_{0.5})_{62}Nb_6M_2B_{30}$ (M = Er, Tb, Y, and Dy) with 2 at. % RE addition extends ΔT from 80 to 130 K [18]. More interesting, a good thermoplastic-forming ability has been found in both Fe–B–Nb-RE [19] and (CoFe)–Nb-M-B [18] MGs. Despite of these facts, the underlying mechanism for the thermoplastic deformation of Fe-based MGs at the temperature around T_g is not clear.

It is proposed that the total strain of a bulk MG caused by structural relaxation contains three components corresponding to the elastic deformation (ε_E), anelastic deformation (ε_A), and viscoplastic deformation (ε_V) during a room temperature loading-unloading cycle [20,21]. The anelastic deformation can induce internal friction, which gradually converts the mechanical energy of the MG into internal energy during the engineering application process, which greatly affects the life of the material and its use effect [22]. The internal friction of Fe-based MGs that comes from the anelastic deformation at room temperature has been studied thoroughly in previous work [23,24], but the mechanism of anelastic deformation with the elevated temperature is under disclosure.

In this work, the creep under submicrometer contacts of the Tb-doped $Fe_{66}Tb_5Nb_6B_{23}$ bulk MGs was investigated by nano-indentation at the temperatures ranging from room temperature

* Corresponding author.
** Corresponding author.
E-mail addresses: yuanchenchenneu@hotmail.com (C.C. Yuan), blshen@seu.edu.cn (B.L. Shen).

https://doi.org/10.1016/j.jallcom.2020.157233
0925-8388/

(298 K) to 723 K. The classic relaxation kinetics is observed accompanied with the increase of activation energy upon increasing loading rate, which reveals the high impact of anelastic deformation on the mechanical behavior of RE elements-doped Fe-based MGs. The viscoplastic flow and softening behavior at the temperature approaching T_g is closely related to the relaxation process with a short characteristic time. By comparison of mechanical and thermodynamic properties among different temperatures, this study contributes to the exploration of suitable operating temperature and loading stress in engineering applications, e.g. thermoplastic nanomoulding. More critically, as an important factor affecting the failure behavior of materials, an in-depth study of the anelasticity is of the great importance for the improvement of the material life and the reduction of the internal friction in service processes.

2. Experimental

$Fe_{66}Tb_5Nb_6B_{23}$ MG samples were prepared with nominal compositions by arc-melting of mixing pure Fe (99.99 wt %), Tb (99.9 wt %), Nb (99.95 wt %), and B (99.99 wt %) in a high-purity argon atmosphere. The dimension of indentation specimens is $2 \times 10 \times 1.5$ mm^3. The top side of specimens with the dimension of 2×10 mm^2 was mechanically polished to mirror finish for the nanoindentation experiment. The micro-creep tests at the temperatures of 300, 432, 573, and 723 K were conducted using a NanoTest Vantage (Micro Materials Ltd) with a standard Berkovich diamond indenter. A standard fused silica sample was utilized for nanoindentation tests with the machine compliance calibration for the transducer-tip configuration and tip area functional calibration before each measurement. The load and displacement resolutions are 750 nN and 0.3 nm, respectively. The thermal drift correction was carried out during the unloading process by using post-indentation model. After the creep measurement, the sample was unloaded to 5 mN and holding for 20 s to derive the thermal drift rate of the instrument. The surface morphology around the indents was recorded by Veeco Dimension ICON AFM. At least five indentation tests were carried out under each condition to discard the biased results that are significantly against the others. The amorphous nature and thermal properties of the specimen was check before nanoindentation by X-ray diffraction (XRD, Bruker D8 Discover diffractometer) with Cu K_α radiation and NETZSCH 404 F3 differential scanning calorimeter (DSC) at a heating rate of 40 K/min.

3. Results and discussion

Fig. 1 show XRD pattern and DSC trace of $Fe_{66}Tb_5Nb_6B_{23}$ alloy system. It can be seen from Fig. 1(a) that the XRD pattern of this sample does not show sharp characteristic diffraction peaks, but only one diffuse scattering peak appears at around 45°, which shows that during the casting process, $Fe_{66}Tb_5Nb_6B_{23}$ bulk MG have not crystallized. The result suggests amorphous feature, and subsequent DSC experiments further confirmed the amorphous nature of the sample. The DSC curve of $Fe_{66}Tb_5Nb_6B_{23}$ bulk MG at a temperature rise rate of 40 K/min in the temperature range from 600 to 1220 K is shown in Fig. 1(b). An obvious glass transition with a wide supercooled liquid region is clearly seen. The glass transition temperature (T_g) and the onset temperature of crystallization (T_x) are marked in Fig. 1(b). The T_g is 886 K, which is about 588 K higher than room temperature. Different exothermic peaks that appear at 979, 1085 and 1126 K, respectively, corresponding to the precipitation of different crystalline phases. The supercooled liquid region ($\Delta T_x = T_x - T_g$) is about 93 K, which is widened about 138% by adding a minor RE elements as compared with the composition of $Fe_{71}Nb_6B_{23}$ ($\Delta T_x = 39$ K) [10]. It indicates that the minor RE element

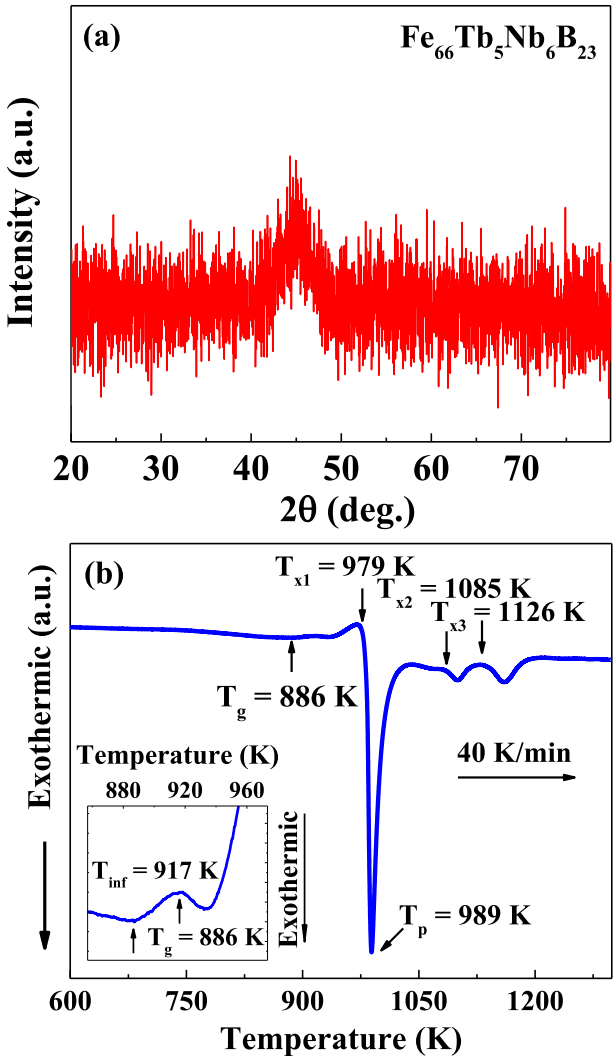

Fig. 1. The XRD pattern (a) and DSC curve (b) of the as-cast $Fe_{66}Tb_5Nb_6B_{23}$ bulk MG.

addition is effective for improving the thermostability of the Fe—Nb—B alloy system. The abnormal exothermic peak (marked as T_{inf}) is also observed in the supercooled liquid region for this alloy, as shown in the magnified view of the thermal traces near T_g of Fig. 1(b). This phenomenon has been well discussed in our recent work that may be attributed to the structural distortion induced by the addition of atoms with large size [15,17]. Tb microalloying causes slightly different crystallization behaviors as compared with other $Fe_{66}RE_5Nb_6B_{23}$ MGs containing Dy, Ho, Er, and Tm [17]. A pronounced exothermic peak after the glass transition corresponds to the precipitation of a single phase. No shoulder-like peak or splitting has been found in the main exothermic peak as observed in the Ho-containing $Fe_{66}Ho_5Nb_6B_{23}$ [17]. It demonstrates that the competition between $Fe_{23}B_6$, Fe_3B and $RE_2Fe_{14}B$ phases is impeded in the first stage of the crystallization process in the $Fe_{66}Tb_5Nb_6B_{23}$ MG.

The load-displacement (P-h) curves of $Fe_{66}Tb_5Nb_6B_{23}$ MG at loading rates of 1, 5, 10, 50 and 100 mN s^{-1} are shown in Fig. 2 (a) - (d). The load-unload sequence can be clearly seen in Fig. 2. The sample was firstly loaded to a limit of 50 mN, holding for 100s, then completely unloaded to zero at the same rate as the loading rate. The obvious serration behavior along with the typical pop-in phenomenon is observed in the sample measured at temperatures of 423 and 527 K during the loading process with a constant loading

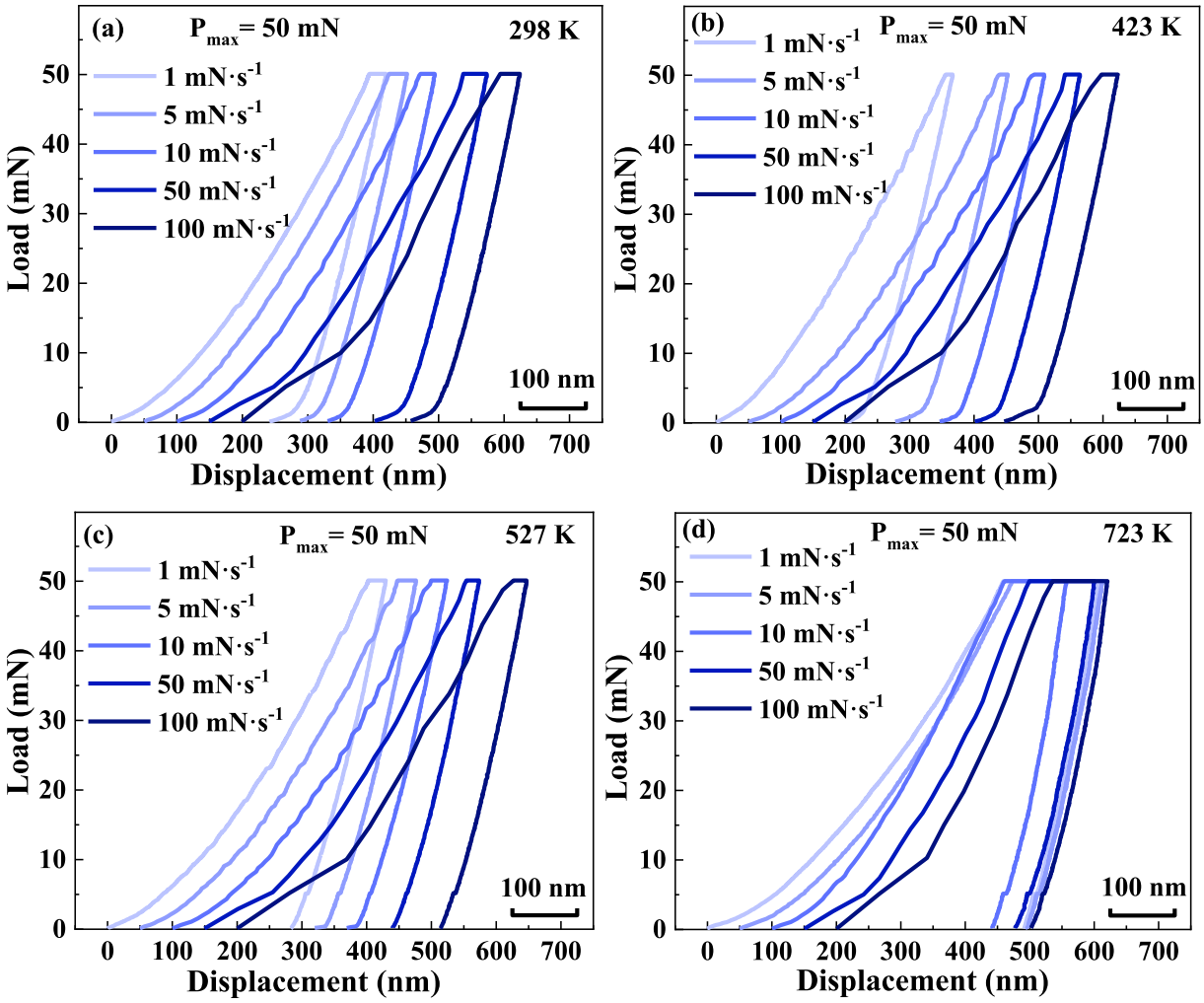

Fig. 2. Load - displacement (P - h) curves of the $Fe_{66}Tb_5Nb_6B_{23}$ MG under different loading rates **with the peak load of** 50 mN at temperature of 298 (room temperature), 423, 527, and 723 K, respectively.

rate lower than 50 mN s^{-1}, see Fig. 2 (b) and (c). It is consistent with the work of Song et al. [25] who observed in situ the regular slip stripes in the cross section of the sample after the shear band slip using a high-speed camera, and confirms that the serrated flow is the result of intermittent slip of the shear band. Previous studies show that the serrated flow strongly depends on the temperature and strain rate of the amorphous alloy during deformation [26,27], which relates to the formation and propagation of shear bands closely [28]. At 723 K, serrated flow disappears at all loading rates, see Fig. 2(d). That can be ascribed to the improved atomic motion with the rise of temperature. In this case, the multiple shear bands can be generated at the same time, which results in a more uniform plastic deformation along with the disappearance of serrated flow.

The creep displacement curves during the load holding period of $Fe_{66}Tb_5Nb_6B_{23}$ MG at measured temperatures of 298, 432, 573, and 723 K with a load limit of 50 mN are displayed in Fig. 2 (a)–(d). With increasing load rate from 1 to 100 mN s^{-1}, the maximum indentation depth during load holding period increases from less than 5 to close to 50 nm at room temperature. The maximum indentation depth increases remarkably with increasing temperature as well. The hardness (H) and elastic modulus (E) derived from nanoindentation at the loading rate ranging from 1 to 100 mN s^{-1} are listed in Table 1. It can be seen that both E and H decrease dramatically with increasing temperature, especially at the temperature of 723 K. Compared with the sample measured at room temperature, the H is reduced more than 50%, and the E decreases about 14% at the loading rate of 5 mN s^{-1} measured at 723 K, suggesting a softening effect of $Fe_{66}Tb_5Nb_6B_{23}$ MG at the temperature approaching to T_g.

The anelastic flow of a MG often occurs in the elastic region below the yield stress, which closely related to the non-equilibrium characteristics of amorphous solids. Unlike the plastic flow behavior of MGs, anelastic flow is relatively uniform on the macroscopic scale, generally no shear band propagates [29]. Typical anelastic flow occurs when a metallic glass is dynamically loaded and unloaded in the elastic region, and it appears as a hysteresis loop of the stress-strain curve. As reported by Park and Lu et al. [30,31], anelastic deformation can be observed during the nanoindentation period of quick loading and unloading, while the viscoplastic deformation occurs when a MG is subjected to long-term stress loading (creep). Hence, the total strain of $Fe_{66}Tb_5Nb_6B_{23}$ MG includes the elastic deformation ε_E, the anelastic deformation ε_A and the viscoplastic deformation ε_V. ε_A and ε_V gradually increase with increasing stress holding time and eventually reach a saturated state. When the stress is completely unloaded, the elastic part ε_E and the anelastic part ε_A completely disappear, only remaining the viscoplastic part ε_V [20]. Based on the above theoretical study, the displacements of the indenter into the sample during load

Table 1
Hardness H and elastic modulus E of the $Fe_{66}Tb_5Nb_6B_{23}$ MG as a function of loading rates measured at different temperatures.

Loading rate ($mN \cdot s^{-1}$)	H (GPa)				E (GPa)			
	298 K	423 K	573 K	723 K	298 K	423 K	573 K	723 K
1	12.5 ± 0.6	14.4 ± 2.3	10.5 ± 1.1	5.2 ± 0.6	194.5 ± 5.1	219.9 ± 35.5	193.8 ± 5.6	177.2 ± 7.9
5	13.7 ± 0.8	13.5 ± 1.0	11.0 ± 1.5	6.6 ± 1.0	205.7 ± 5.6	204.0 ± 5.9	193.1 ± 7.8	177.0 ± 12.7
10	13.3 ± 0.7	13.7 ± 2.5	10.5 ± 1.1	11.9 ± 6.2	205.8 ± 2.9	210.1 ± 25.0	195.9 ± 7.0	245.8 ± 42.3
50	12.6 ± 1.2	12.1 ± 1.2	11.0 ± 1.4	9.2 ± 1.6	202.0 ± 6.8	205.2 ± 9.4	198.0 ± 8.0	227.5 ± 18.9
100	11.6 ± 0.8	12.0 ± 0.6	9.8 ± 0.6	11.5 ± 1.4	204.4 ± 9.3	205.9 ± 5.4	197.6 ± 8.8	263.4 ± 10.3

holding period can be described by a classic relaxation kinetics equation, plus the viscoplastic contribution $\frac{t}{\mu_0}$ [21]:

$$h = h_0\left(1 - e^{-\frac{t}{\tau}}\right) + \frac{t}{\mu_0} \quad (1)$$

where t is the creep time, h_0 the ultimate additional displacement that occurs during the constant-load period, τ the characteristic relaxation time of a Kelvin unit, and μ_0 the viscoplastic constant in a Maxwell dashpot. Fig. 3 show the typical experimental and fitted creep displacement curves of $Fe_{66}Tb_5Nb_6B_{23}$ at the loading rate of 5 mN s^{-1}. It is can be seen with increasing temperature from 298 to 727 K, the maximum penetration of the indenter increases obviously from 26 to 140 nm. The fitting parameters are listed in Table 2. The h_0 that represents the final indentation depth after the loading holding period increases strikingly with increasing loading rate, reaching a maximum value of 16 nm at the loading rate of 50 mN s^{-1}. It drops about 33% with further increasing the loading rate to 100 mN s^{-1}. However, at the temperature higher than room temperature such as 423 K, the h_0 is similar at all loading conditions, independent of the loading rate. With further increasing temperature to higher than 573 K, the h_0 decreases with increasing loading rate. The τ shows a resembling loading-rate dependency as h_0 at different temperatures. The μ_0^{-1} as an indicator of viscoplastic deformation of the sample, seems independent of loading rates. With increasing temperature from 298 to 723 K, the μ_0^{-1} increases from 0.07 to 0.49 at the loading rate of 5 mN s^{-1}. It indicates that the viscoplastic deformation is more dominant at a temperature that close to T_g.

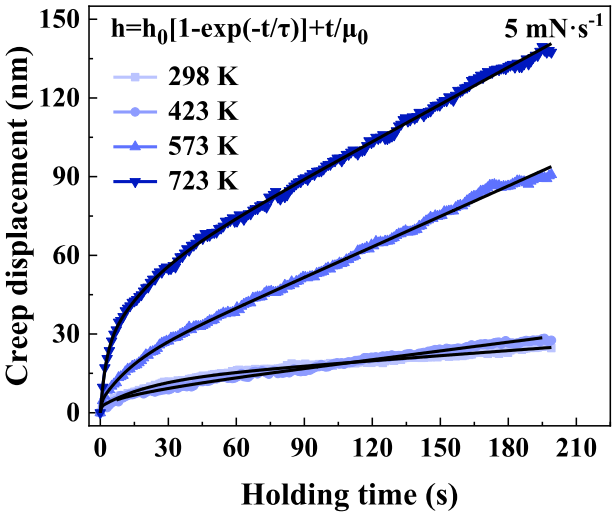

Fig. 3. Experimental and fitted creep displacement curves of the $Fe_{66}Tb_5Nb_6B_{23}$ MG under a loading rate of 5 mN s^{-1} with the peak load of 50 mN at different temperatures by using the classic relaxation kinetics equation.

Table 2
The fitting parameters of the creep displacement curves of the $Fe_{66}Tb_5Nb_6B_{23}$ MG at different temperatures using the classic relaxation kinetics equation.

	Loading rate ($mN \cdot s^{-1}$)	h_0 (nm)	τ (s)	μ_0^{-1} (nm s^{-1})
298 K	1	8.78 ± 0.11	11.04 ± 0.48	0.06
	5	11.58 ± 0.15	16.27 ± 0.58	0.07
	10	14.88 ± 0.20	17.74 ± 0.61	0.06
	50	16.07 ± 0.20	18.27 ± 0.58	0.07
	100	10.76 ± 0.11	14.40 ± 0.44	0.05
423 K	1	3.74 ± 0.07	4.45 ± 0.51	0.05
	5	6.93 ± 0.13	10.43 ± 0.73	0.11
	10	8.14 ± 0.16	10.63 ± 0.77	0.06
	50	7.59 ± 0.09	6.69 ± 0.39	0.09
	100	4.37 ± 0.14	5.55 ± 0.98	0.12
573 K	1	11.80 ± 0.39	19.73 ± 1.55	0.19
	5	16.32 ± 0.24	9.27 ± 0.54	0.39
	10	11.68 ± 0.22	5.85 ± 0.59	0.13
	50	5.73 ± 0.19	5.36 ± 1.01	0.18
	100	7.12 ± 0.13	3.31 ± 0.45	0.13
723 K	1	44.34 ± 0.45	18.74 ± 0.47	0.88
	5	43.61 ± 0.33	7.68 ± 0.26	0.49
	10	36.32 ± 0.25	4.74 ± 0.20	0.30
	50	24.66 ± 0.35	4.20 ± 0.38	0.34
	100	15.69 ± 0.25	3.24 ± 0.39	0.33

Since the relaxation time decreases with increasing temperature, the anelastic flow is thermally activated, each value of the distribution of the characteristic relaxation time as function of temperature follows the equation:

$$\tau = \tau_0 e^{-\frac{Q}{kT}} \quad (2)$$

where Q is the activation energy of the relaxation process, τ_0 a preexponential factor, k Boltzmann's constant, and T the absolute temperature. The logarithm plots of the relaxation time as a function of $1/T$ at each loading rate are displayed in Fig. 4. Keeping the invariability of loading rates, fitting four sets of data at different temperatures, it is found that they basically conform to the linear relationship. Referring to Eq. (2), the relaxation activation energy Q can be derived. According to Eq. (2), an effective activation energy can be evaluated to be 0.032 eV $atom^{-1}$ at a loading rate of 5 mN s^{-1}. It increases gradually to 0.069 eV with increasing loading rate from 5 to 100 mN s^{-1}. These values are much smaller than, for example, the energy of a vacancy formation in a Fe-based crystalline alloy. As reported by A. Hernando et al. [32], the activation energy of relaxation process of $(Fe_{0.05}Co_{0.95})_{75}Si_{15}B_{10}$ is around 0.15eV, a little higher than what we found. The amount of the creep activation is 3–4 times that of the stress relaxation, i.e., it has much fewer atoms that participate in stress relaxation as compared with the creep process [33].

MG-forming alloy systems are considered to be structurally heterogeneous at the subnano-to nanoscale [34–37], especially in RE-added Fe-based MGs [34]. The nanoscale heterogeneity based on the core-shell-like model [29] can be characterized two relaxation processes during the creep deformation with different relaxation times. Therefore, here a Maxwell unit with two Kelvin

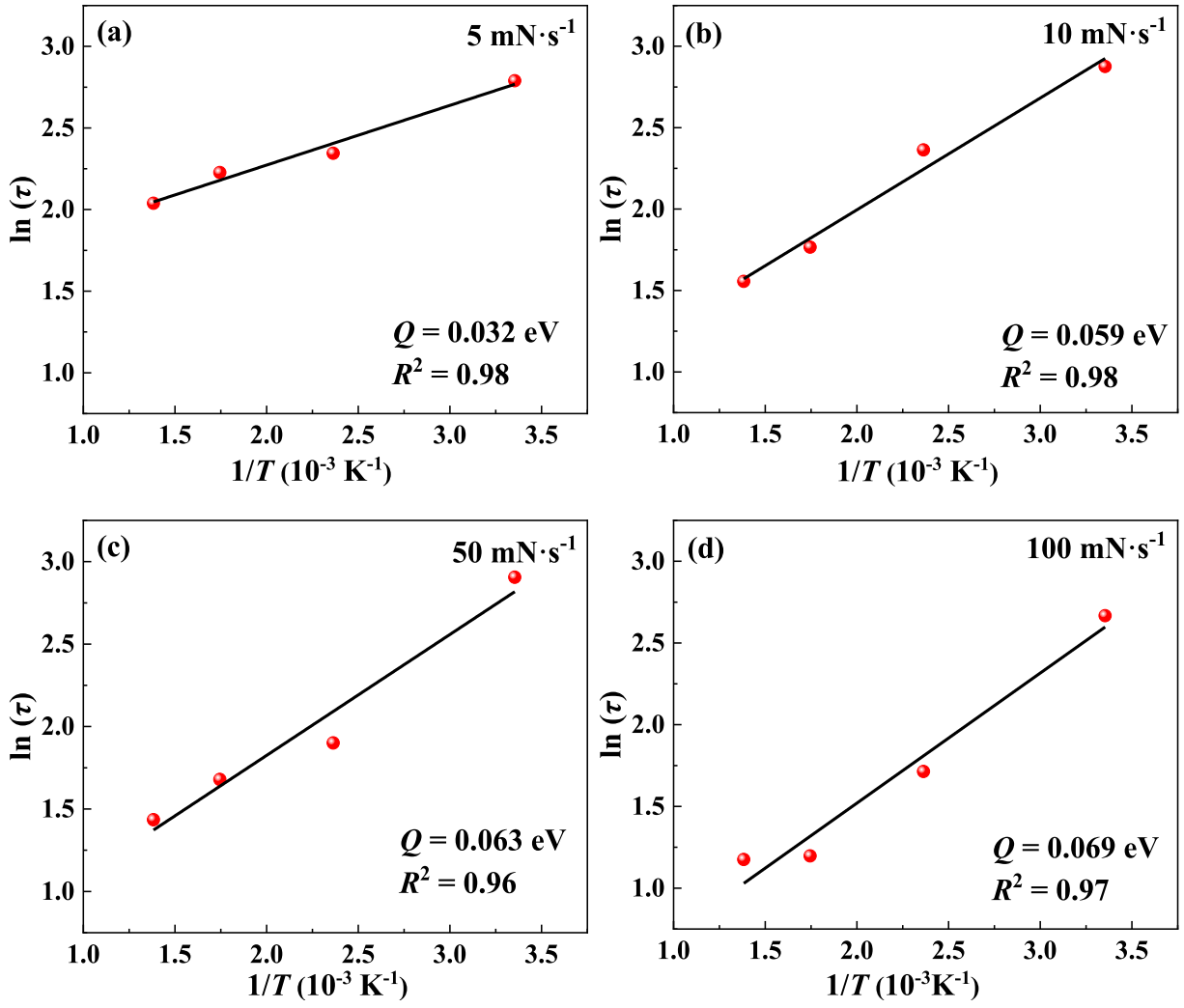

Fig. 4. Logarithm of the mean of the observed relaxation times τ at each temperature as a function of $1/T$, under the loading rates of 5–100 mN s^{-1}. The relaxation activation energy Q **and the fitting correlation coefficient** R^2 **are shown in the lower right corner of each picture. The straight line is a fit to the data.**

units connected in series under the frame of the Maxwell-Voigt model is utilized for the analysis of the creep displacement as well [20]:

$$h = h_1\left(1 - e^{-\frac{t}{\tau_1}}\right) + h_2\left(1 - e^{-\frac{t}{\tau_2}}\right) + \frac{t}{\mu_0} \quad (3)$$

where the parameters h_1, τ_1 and h_2, τ_2 correspond to two separated relaxation processes. h_1 and τ_1 represent the displacement and relaxation time of the first Kelvin unit, while h_2 and τ_2 represent that of the second Kelvin unit. As shown in Fig. 5, the creep data of the sample measured at the temperature of 727 K at the loading rate of 1 mN s^{-1} can be accurately described by Eq. (3), where the correlation coefficient R^2 is 99.95. Since the structural inhomogeneity can be described by a two-phase model in MGs that includes a strongly bonded hard region and a weakly bonded soft region [29], 2 K units represent the anelastic relaxation process of soft and hard regions, respectively. A Maxwell unit is used to characterize the viscoplastic deformation.

Fig. 6 (a) and (b) shows the experimental and fitted creep curves of the $Fe_{66}Tb_5Nb_6B_{23}$ MG as a function of loading rates and temperatures. It can be seen that the typical creep curves can be fitted

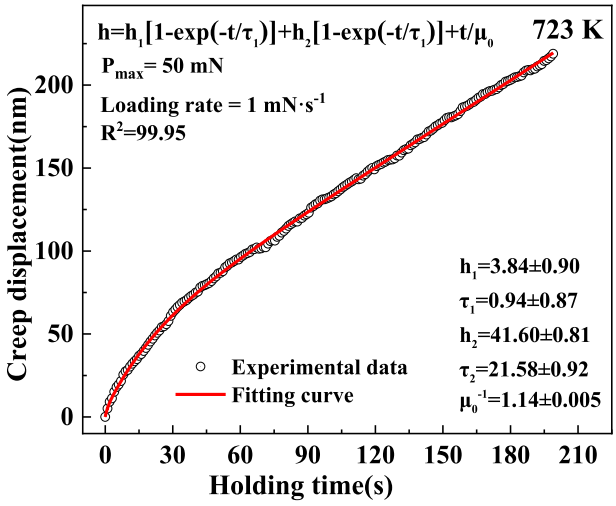

Fig. 5. Experimental and fitted creep displacement curves of the $Fe_{66}Tb_5Nb_6B_{23}$ MG under a loading rate of 1 mN s^{-1} with the peak load of 50 mN at 723 K by using the Maxwell-Voigt model.

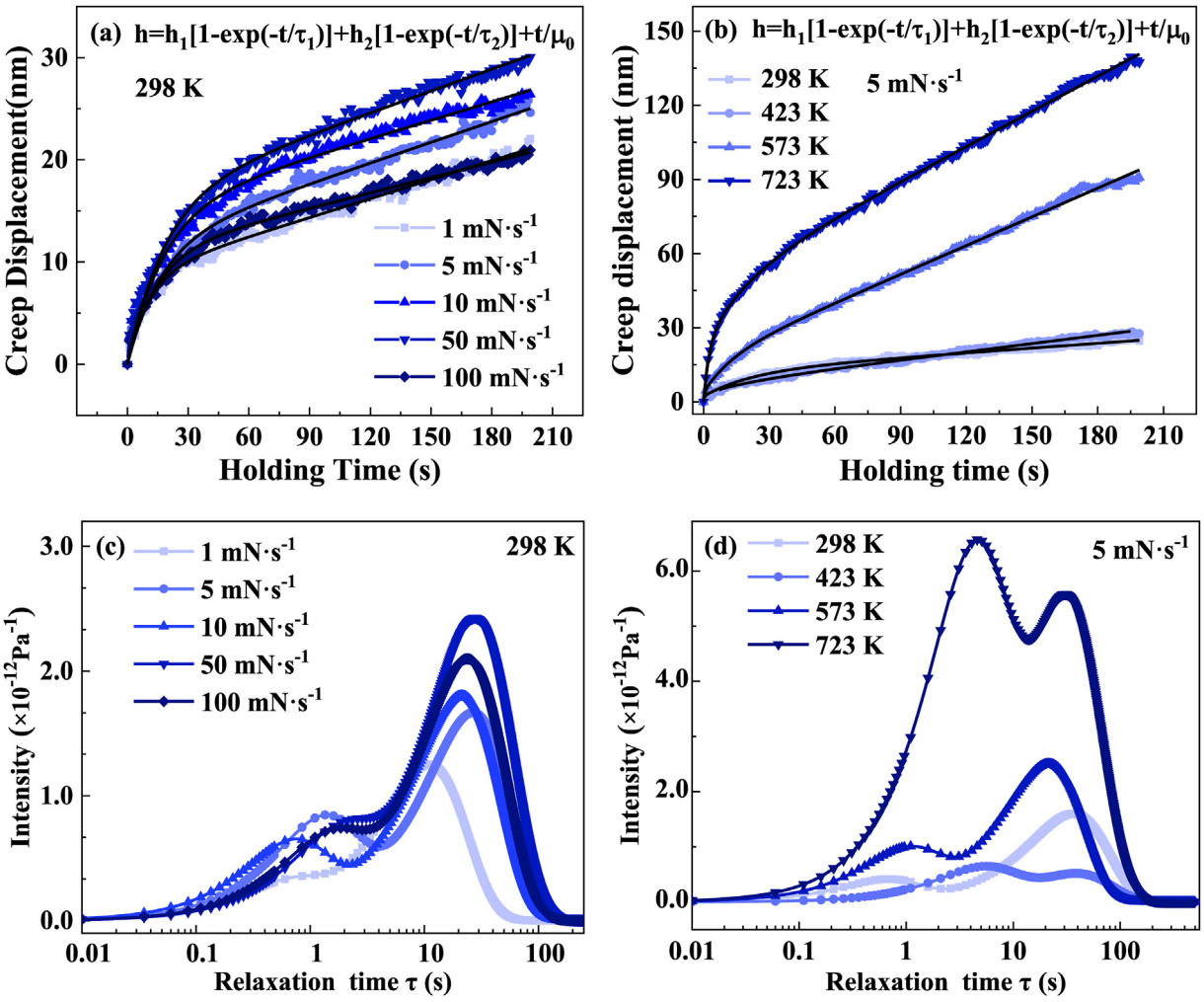

Fig. 6. (a) and (b) The creep displacement and fitting curves of the $Fe_{66}Tb_5Nb_6B_{23}$ MG during the load holding period measured under room temperature at different loading rates (a) and measured under the loading rate of 5 mN s^{-1} at different temperatures (b). (c) and (d) The relaxation spectra of the $Fe_{66}Tb_5Nb_6B_{23}$ MG measured at 298 K under different loading rates (c), and measured under the loading rate of 5 mN s^{-1} at different temperatures (d) based on the anelastic part of the creep displacement curves.

successfully using Maxwell-Voigt model. The fitting parameters for the creep displacement-time (h-t) curve at different loading rates and temperatures are listed in Table 3. At room temperature, the μ_0^{-1} that represents the viscoplastic deformation ability of MGs almost keep a constant, independent of loading rates, which is in good agreement with previous research results [38]. While the μ_0^{-1} increases from 0.02 to 0.11 with increasing loading rate from 5 to 100 mN s^{-1} at 423 K. With further increasing temperature, the μ_0^{-1}, on the contrary, decreases obviously from 0.39 to 0.31 and 0.87 to 0.22 nm s^{-1} with increasing loading rate at 573 and 723 K, respectively, exhibiting a work hardening with an enhanced viscosity. The displacements h_1 and h_2 of two Kelvin units during primary and secondary relaxation processes increase significantly with increasing temperature, accompanied by a large fluctuation of the relaxation time τ_1 and τ_2.

Coincidence with the previous work [37,38], the creep displacement with extended loading time as displayed in Fig. 6 (a) and (b) is in direct proportion with temperatures and loading rates. The anelastic component of a creep process can be analyzed in terms of relaxation time spectrum using the approximate equation as suggested in the work of Castellero et al. [39,40]:

$$L(\tau) = \left[\sum_{i=1}^{n}\left(1+\frac{t}{\tau_i}\right)\frac{h_i}{\tau_i}e^{-\frac{t}{\tau_i}}\right]\frac{A_0}{P_0 h_{in}}t|_{t=2\tau} \quad (4)$$

where L is the spectrum intensity, A_0/P_0 the inverse of the hardness, and h_{in} the maximum indentation depth. Fig. 6 (c) and (d) presents the relaxation spectra of the $Fe_{66}Tb_5Nb_6B_{23}$ MG as a function of loading rates and temperatures. Two separate relaxation peaks can be observed in all relaxation spectra. According to the core-shell model [31], the first peak with short relaxation times in the relaxation spectrum represents the defects in the hard region, while the second peak with long relaxation times represents the defects in the soft region. Based on the definition of flow defects, the structural rearrangement with a longer relaxation time than that of elastic matrix to can dissipate the stress concentrates around the elastic matrix. Such process can be well described by Kelvin units [41], corresponding to the inelastic deformation of MGs. With increasing the loading rate from 1 to 50 mN s^{-1}, both the intensity and relaxation time of the first and second peaks alter

Table 3
The fitting parameters of the creep displacement curves of the $Fe_{66}Tb_5Nb_6B_{23}$ MG using the Maxwell-Voigt model measured at different temperatures.

	Loading rate ($mN \cdot s^{-1}$)	h_1 (nm)	τ_1 (s)	h_2 (nm)	τ_2 (s)	μ_0^{-1}(nm/s)
298 K	1	1.3 ± 0.4	0.7 ± 0.8	7.7 ± 0.4	13.6 ± 1.1	0.06
	5	4.5 ± 0.3	1.5 ± 0.3	10.9 ± 0.3	33.0 ± 2.4	0.11
	10	3.3 ± 0.2	0.8 ± 0.3	10.9 ± 0.2	26.3 ± 1.2	0.09
	50	2.8 ± 0.3	1.9 ± 0.5	14.1 ± 0.3	34.2 ± 1.7	0.08
	100	2.8 ± 0.2	1.6 ± 0.4	12.2 ± 0.2	29.5 ± 1.3	0.05
423 K	1	1.8 ± 0.9	1.4 ± 1.1	2.0 ± 0.9	8.9 ± 3.8	0.05
	5	2.9 ± 0.6	0.7 ± 0.5	2.0 ± 0.6	10.1 ± 3.9	0.02
	10	2.6 ± 0.4	0.4 ± 0.6	5.9 ± 0.4	17.1 ± 2.3	0.06
	50	1.6 ± 0.5	0.3 ± 0.9	6.1 ± 0.5	8.5 ± 0.9	0.09
	100	0.16 ± 5.0	0.1 ± 2406.3	2.8 ± 5.0	1.6 ± 1.9	0.11
573 K	1	2.9 ± 0.5	0.6 ± 0.8	10.0 ± 0.6	30.5 ± 4.8	0.18
	5	4.0 ± 0.9	0.6 ± 0.6	12.8 ± 0.8	13.2 ± 1.5	0.39
	10	5.7 ± 1.7	1.4 ± 0.8	6.5 ± 1.6	11.9 ± 3.5	0.31
	50	2.1 ± 2.4	1.2 ± 2.4	3.7 ± 2.3	8.2 ± 5.1	0.18
	100	2.2 ± 1.9	1.0 ± 1.8	8.5 ± 1.8	8.7 ± 2.1	0.13
723 K	1	3.8 ± 0.9	0.9 ± 0.9	41.6 ± 0.8	21.6 ± 0.9	0.87
	5	18.4 ± 1.0	1.4 ± 0.2	37.6 ± 0.9	25.8 ± 1.4	0.57
	10	9.4 ± 1.6	0.5 ± 0.4	30.6 ± 1.5	9.3 ± 0.7	0.65
	50	18.6 ± 0.6	1.4 ± 0.2	14.5 ± 0.6	33.4 ± 3.7	0.45
	100	8.7 ± 1.1	0.6 ± 0.5	21.5 ± 1.1	26.2 ± 3.2	0.22

remarkably. The relaxation spectrum is a statistical result of the relaxation process of two different characteristic relaxation time in the system, essentially, corresponding to each peak as marked in Fig. 6 (c) and (d). The higher the peak intensity, the more the relaxation processes of the characteristic relaxation time involved, i.e., more defects are activated. The increase of the peak intensity with increasing loading rate indicates the generation of more defects at a higher loading rate. Compared with the primary relaxation peak, the variation of the secondary relaxation peak in the $Fe_{66}Tb_5Nb_6B_{23}$ MG is more pronounced. As shown in Fig. 6 (c), the intensity of the secondary relaxation process increases gradually with increasing loading rate, accompanied with the shift of the peak position to a longer time region. It indicates that the defects with longer relaxation times intended to be activated at higher loading rates, e.g. in a low-velocity impact mode, at room temperature, which is consistent with the increase of the activation energy with increasing loading rate as shown in Fig. 4. More interestingly, it is found that both the creep displacement and the intensity of relaxation spectra is reduced at the loading rate of 100 mN s^{-1}. This abnormal change of relaxation peaks may be due to the saturation of the activated defects during the creep deformation at a loading rate of 50 mN s^{-1} [38], see Fig. 6 (a) and (c).

Differ from the relaxation spectra at the temperature close to room temperature, the obvious increase of the first relaxation peak at 723 K with the loading rate of 5 mN s^{-1} can be clearly seen in Fig. 6 (d). Meanwhile, the peak of the primary relaxation is more intense than that of the secondary relaxation at this temperature. It indicates that the participation of the relaxation process with a short relaxation time is more important during the plastic deformation. The short-time relaxation is due to the high restriction of the atom's movement. Such restriction is mainly attributed to the relatively strong chemical interaction between atoms and the network-like configuration hided in the glassy matrix, i.e., the formation of the hard region. The breakage of the atomic bonding at high temperature results in the fast motion of atoms, which is beneficial for the superplastic flow of MGs. As shown in Fig. 6 (c) and (d), the defects in the strongly-bonded hard region related to the shorter relaxation time more prefer to be activated at the temperature close to T_g, e.g., 723 K, while the defects in the weakly-bonded soft region related to the longer relaxation time are intend to be activated at room temperature. Thus, it can be concluded that the high temperature and low loading rate used in the present indentation experiments favor the anelastic deformation process with a shorter relaxation time, the one with longer i.e., with larger activation energy Q failing to be activated and therefore not taking part in the recovery [42]. Moreover, at the high temperature, the penetration during the constant-load segment decreases because the characteristic relaxation time is so short that the partial anelastic recovery can occur during the loading process.

The activation of a large number of dynamic defects with a short characteristic relaxation at 723 K is also consistent with the pronounced softening phenomenon as demonstrated by the obvious decrease of both hardness and elastic modulus at this temperature. As proposed by Hufnagel [43] and Ma [44] et al., the elastic modulus represents the inherent stiffness of atomic bonds. The atomic-scale defects inside the system activated along with elevated temperature will reduce the energy barrier for atom motion and induce the breakage of atomic bonds, which eventually leads to the softening of glass matrix. It, macroscopically, turns out that the elastic modulus and the hardness decrease.

The structural evolution during the plastic deformation can be regarded as a process of competition between the two mechanisms of shear-induced free volume generation and diffusion-induced free volume annihilation. The increase in temperatures leads to the generation and activation of defects such as internal compositional inhomogeneity or atomic agglomeration, which leads to a significant reduction in the actual occupied volume of atoms, and thus excess free volume. During the superplastic deformation, the rate of free volume generation is much higher than the rate of free volume annihilation caused by diffusion. The potential energy of the disordered system will increase, accordingly. It finally leads to the notable softening phenomenon along with the structural rejuvenation.

4. Conclusions

The micro-creep behaviors of the $Fe_{66}Tb_5Nb_6B_{23}$ MG at different temperatures were investigated by using nanoindentation. Anelastic and viscoplastic deformation mechanism during the creep process of $Fe_{66}Tb_5Nb_6B_{23}$ were discussed in details. The creep displacement and strain rate curves during the constant load holding period can be well described by the Maxwell-Voigt model with one or two Kelvin units. The activation energy of the relaxation process evaluated under a classic relaxation kinetics is dependent on loading rates, which increases gradually from 0.032 to 0.069 eV with increasing loading rate from 5 to 100 mN s^{-1}. Based on the relaxation time spectra under the frame of the two-

phase model, it is found that the defects with a short relaxation time are more dominant in the plastic flow process with the elevated temperature, especially at a high temperature of 723 K. The hardness and elastic modulus were reduced significantly as well when the sample was heated from room temperature to 723 K, demonstrating a pronounced softening behavior. The present work may help us in deeply understand the elastoplasticity of MGs at room temperature as well as the temperature close to T_g.

CRediT authorship contribution statement

C.C. Yuan: Conceptualization, Visualization, Writing - original draft, Writing - review & editing, Project administration, Funding acquisition, Supervision. **R. Liu:** Methodology, Data curation, Writing - original draft. **C.M. Pang:** Methodology, Investigation, Data curation. **X.F. Zuo:** Investigation. **B.F. Li:** Investigation. **S.C. Song:** Investigation. **J.Y. Hu:** Investigation. **W.W. Zhu:** Methodology. **B.L. Shen:** Funding acquisition.

Declaration of competing interest

The authors declare that they have no known competing financial interests or personal relationships that could have appeared to influence the work reported in this paper.

Acknowledgments

This work was supported by the National Natural Science Foundation of China (Grant Nos. 52071078, 51631003 and 51601038), the Natural Science Foundation of Jiangsu Province, China (Grant No. BK20171354), Postgraduate Research & Practice Innovation Program of Jiangsu Province (Grant No. SJCX20_0038), the Fundamental Research Funds for the Central Universities (Grant No. 2242020K40002), Jiangsu Key Laboratory for Advanced Metallic Materials (Grant No. BM2007204).

References

[1] G. Kumar, H.X. Tang, J. Schroers, Nanomoulding with amorphous metals, Nature 457 (7231) (2009) 868–872.
[2] J. Schroers, On the formability of bulk metallic glass in its supercooled liquid state, Acta Mater. 56 (3) (2008) 471–478.
[3] M.M. Trexler, N.N. Thadhani, Mechanical properties of bulk metallic glasses, Prog. Mater. Sci. 55 (2010) 759–839.
[4] J. Lu, G. Ravichandran, W.L. Johnson, Deformation behavior of the $Zr_{41.2}Ti_{13.8}Cu_{12.5}Ni_{10}Be_{22.5}$ bulk metallic glass over a wide range of strain-rates and temperatures, Acta Mater. 51 (12) (2003) 3429–3443.
[5] T. Nieh, J. Wadsworth, Homogeneous deformation of bulk metallic glasses, Scripta Mater. 54 (3) (2006) 387–392.
[6] G. Wang, J. Shen, J. Sun, Y. Huang, J. Zou, Z. Lu, Z. Stachurski, B. Zhou, Superplasticity and superplastic forming ability of a Zr-Ti-Ni-Cu-Be bulk metallic glass in the supercooled liquid region, J. Non-Cryst. Solids 351 (3) (2005) 209–217.
[7] C. Chiang, J. Chu, C. Lo, T. Nieh, Z.X. Wang, W.H. Wang, Homogeneous plastic deformation in a Cu-based bulk amorphous alloy, Intermetallics 12 (10–11) (2004) 1057–1061.
[8] A.D. Wang, Q.K. Man, M.X. Zhang, H. Men, B.L. Shen, S.J. Pang, T. Zhang, Effect of B to P concentration ratio on glass-forming ability and soft-magnetic properties in $[(Fe_{0.5}Ni_{0.5})_{0.78}\ B_{0.22-x}P_x]_{97}Nb_3$ glassy alloys, Intermetallics 20 (1) (2012) 93–97.
[9] B. Shen, M. Akiba, A. Inoue, Effects of Si and Mo additions on glass-forming in FeGaPCB bulk glassy alloys with high saturation magnetization, Phys. Rev. B 73 (10) (2006), 104204.
[10] J.H. Yao, H. Yang, J. Zhang, J.Q. Wang, The influence of Nb and Zr on glass-formation ability in the ternary Fe-Nb-B and Fe-Zr-B and quaternary Fe-(Nb, Zr)-B alloy systems, J. Mater. Res. 23 (2008) 392–401.
[11] A. Inoue, B. Shen, Soft magnetic bulk glassy Fe-B-Si-Nb alloys with high saturation magnetization above 1.5 T, Mater. Trans. 43 (2002) 766–769.
[12] Z. Han, J. Zhang, Y. Li, Quaternary Fe-based bulk metallic glasses with a diameter of 5 mm, Intermetallics 15 (2007) 1447–1452.
[13] J.F. Li, Y. Shao, X. Liu, K.F. Yao, Fe-based bulk amorphous alloys with high glass formation ability and high saturation magnetization, Sci. Bull. 60 (2015) 396–399.
[14] D.H. Kim, J.M. Park, D.H. Kim, W.T. Kim, Development of quaternary Fe-B-Y-Nb bulk glassy alloys with high glass-forming ability, J. Mater. Res. 22 (2) (2007) 471–477.
[15] F. Hu, C.C. Yuan, Q. Luo, W. Yang, B. Shen, Effects of ho addition on thermal stability, thermoplastic deformation and magnetic properties of FeHoNbB bulk metallic glasses, J. Alloys Compd. 807 (2019), 151675.
[16] S. Lee, H. Kato, T. Kubota, K. Yubuta, A. Makino, A. Inoue, Excellent thermal stability and bulk glass forming ability of Fe-B-Nb-Y soft magnetic metallic glass, Mater. Trans. 49 (3) (2008) 506–512.
[17] F. Hu, C. Yuan, Q. Luo, W. Yang, B. Shen, Effects of heavy rare-earth addition on glass-forming ability, thermal, magnetic, and mechanical properties of Fe-RE-B-Nb (RE = Dy, Ho, Er or Tm) bulk metallic glass, J. Non-Cryst. Solids 525 (2019), 119681.
[18] Q. Man, A. Inoue, Y. Dong, J. Qiang, C. Zhao, B. Shen, A new CoFe-based bulk metallic glasses with high thermoplastic forming ability, Scripta Mater. 69 (7) (2013) 553–556.
[19] F. Hu, C. Yuan, Q. Luo, W. Yang, B. Shen, Effects of Ho addition on thermal stability, thermoplastic deformation and magnetic properties of FeHoNbB bulk metallic glasses, J. Alloys Compd. 807 (2019), 151675.
[20] A.I. Taub, F. Spaepen, Ideal elastic, anelastic and viscoelastic deformation of a metallic glass, J. Mater. Sci. 16 (11) (1981) 3087–3092.
[21] A. Concustell, J. Sort, A.L. Greer, M.D. Baró, Anelastic deformation of a $Pd_{40}Cu_{30}Ni_{10}P_{20}$ bulk metallic glass during nanoindentation, Appl. Phys. Lett. 88 (17) (2006), 171911.
[22] C. Wang, Q. Fang, A new experimental method to develop the nonlinear anelastic internal friction peaks appearing around room temperature, Phys. Status Solidi 162 (2) (1997) 587–592.
[23] A. Kursumovic, B. Cantor, Anelastic crossover and creep recovery spectra in $Fe_{40}Ni_{40}B_{20}$ metallic glass, Scripta Mater. 34 (11) (1996) 1655–1660.
[24] C.C. Yuan, Z.W. Lv, C.M. Pang, W.W. Zhu, X.-L. Wang, B.L. Shen, J. Alloys Compd. 806 (2019) 246–253.
[25] S.X. Song, H. Bei, J. Wadsworth, T.G. Nieh, Flow serration in a Zr-based bulk metallic glass in compression at low strain rates, Intermetallics 16 (2008) 813–818.
[26] C.A. Schuh, T.G. Nieh, A nanoindentation study of serrated flow in bulk metallic glasses, Acta Mater. 51 (2003) 87–99.
[27] A. Dubach, F.H. Dalla Torre, J.F. Loeffler, Constitutive model for inhomogeneous flow in bulk metallic glasses, Acta Mater. 57 (2009) 881–892.
[28] J.W. Qiao, Y. Zhang, P.K. Liaw, Serrated flow kinetics in a Zr-based bulk metallic glass, Intermetallics 18 (2010) 2057–2064.
[29] J.C. Ye, J. Lu, C.T. Liu, Q. Wang, Y. Yang, Atomistic free-volume zones and inelastic deformation of metallic glasses, Nat. Mater. 9 (8) (2010) 619–623.
[30] K.W. Park, C.M. Lee, M. Wakeda, Y. Shibutani, M.L. Falk, J.C. Lee, Elastostatically induced structural disordering in amorphous alloys, Acta Mater. 56 (19) (2008) 5440–5450.
[31] Z. Lu, W. Jiao, W.H. Wang, H.Y. Bai, Flow unit perspective on room temperature homogeneous plastic deformation in metallic glasses, Phys. Rev. Lett. 113 (4) (2014), 045501.
[32] A. Hernando, O. Nielsen, V. Madurga, Relaxation processes and pure shear stress creep in a metallic glass ribbon of composition $(Fe_{0.05}Co_{0.95})_{75}Si_{15}B_{10}$, J. Mater. Sci. 20 (6) (1985) 2093–2102.
[33] C. Zhang, J. Qiao, J.-M. Pelletier, Y. Yao, Thermal activation in the $Zr_{65}Cu_{18-}Ni_7Al_{10}$ metallic glass by creep deformation and stress relaxation, Scripta Mater. 113 (2016) 180–184.
[34] J.W. Li, A.N. He, B.L. Shen, Effect of Tb addition on the thermal stability, glass-forming ability and magnetic properties of Fe-B-Si-Nb bulk metallic glass, J. Alloys Compd. 586 (2014) S46–S49.
[35] P. Tsai, K. Kranjc, K.M. Flores, Hierarchical heterogeneity and an elastic microstructure observed in a metallic glass alloy, Acta Mater. 139 (2017) 11–20.
[36] Z. Zhu, Z. Zheng, F. Zhang, Y. Wu, M. Trzaskowski, R. Maier, M.R. Robinson, J.J. McGrath, P.M. Visscher, N.R. Wray, J. Yang, Causal associations between risk factors and common diseases inferred from GWAS summary data, Nat. Commun. 9 (2018) 1–12.
[37] C.C. Yuan, Z.W. Lv, C.M. Pang, X.L. Wu, S. Lan, C.Y. Lu, L.G. Wang, H.B. Yu, J.H. Luan, W.W. Zhu, G.L. Zhang, Q. Liu, X.L. Wang, B.L. Shen, Atomic-scale heterogeneity in large-plasticity Cu-doped metallic glasses, J. Alloys Compd. 798 (2019) 517–522.
[38] H.B. Ke, P. Zhang, B.A. Sun, P.G. Zhang, T.W. Liu, P.H. Chen, M. Wu, H.G. Huang, Dissimilar nanoscaled structural heterogeneity in U-based metallic glasses revealed by nanoindentation, J. Alloys Compd. 788 (2019) 391–396.
[39] A. Castellero, B. Moser, D.I. Uhlenhaut, F.H.D. Torre, J.F. Löffler, Room-temperature creep and structural relaxation of Mg-Cu-Y metallic glasses, Acta Mater. 56 (15) (2008) 3777–3785.
[40] J.D. Ferry, Viscoelastic Properties of Polymers, third ed., John Wiley & Sons, New York, 1980.
[41] H.B. Ke, J.F. Zeng, C.T. Liu, Y. Yang, Structure heterogeneity in metallic glass: modeling and experiment, J. Mater. Sci. Technol. 30 (6) (2014) 560–565.
[42] V. Ocelík, K. Csach, A. Kasardová, V.Z. Bengus, Anelastic deformation processes in metallic glasses and activation energy spectrum model, Mater. Sci. Eng., A 226 (1997) 851–855.
[43] T.C. Hufnagel, R.T. Ott, J. Almer, Structural aspects of elastic deformation of a metallic glass, Phys. Rev. B 73 (2006), 064204.
[44] D. Ma, A.D. Stoica, X.L. Wang, Z.P. Lu, B. Clausen, D.W. Brown, Elastic moduli inheritance and the weakest link in bulk metallic glasses, Phys. Rev. Lett. 108 (8) (2012), 085501.